Geophys. J. Int. (2007) **171,** 11–24 doi: 10.1111/j.1365-246X.2007.03518.x

Surface deformation due to loading of a layered elastic half-space: a rapid numerical kernel based on a circular loading element

E. Pan,[1] M. Bevis,[2] F. Han,[1] H. Zhou[2] and R. Zhu[1]

[1]*Department of Civil Engineering and Department of Applied Mathematics, University of Akron, Akron,* OH 44325*, USA. E-mail: pan2@uakron.edu*
[2]*Department of Geological Sciences, Ohio State University, Columbus,* OH 43210*, USA*

Accepted 2007 June 3. Received 2007 June 1; in original form 2006 November 7

SUMMARY

This study is motivated by a desire to develop a fast numerical algorithm for computing the surface deformation field induced by surface pressure loading on a layered, isotropic, elastic half-space. The approach that we pursue here is based on a circular loading element. That is, an arbitrary surface pressure field applied within a finite surface domain will be represented by a large number of circular loading elements, all with the same radius, in which the applied downwards pressure (normal stress) is piecewise uniform: that is, the load within each individual circle is laterally uniform. The key practical requirement associated with this approach is that we need to be able to solve for the displacement field due to a single circular load, at very large numbers of points (or 'stations'), at very low computational cost. This elemental problem is axisymmetric, and so the displacement vector field consists of radial and vertical components both of which are functions only of the radial coordinate r. We achieve high computational speeds using a novel two-stage approach that we call the sparse evaluation and massive interpolation (SEMI) method. First, we use a high accuracy but computationally expensive method to compute the displacement vectors at a limited number of r values (called control points or knots), and then we use a variety of fast interpolation methods to determine the displacements at much larger numbers of intervening points. The accurate solutions achieved at the control points are framed in terms of cylindrical vector functions, Hankel transforms and propagator matrices. Adaptive Gauss quadrature is used to handle the oscillatory nature of the integrands in an optimal manner. To extend these exact solutions via interpolation we divide the r-axis into three zones, and employ a different interpolation algorithm in each zone. The magnitude of the errors associated with the interpolation is controlled by the number, M, of control points. For $M = 54$, the maximum RMS relative error associated with the SEMI method is less than 0.2 per cent, and it is possible to evaluate the displacement field at 100 000 stations about 1200 times faster than if the direct (exact) solution was evaluated at each station; for $M = 99$ which corresponds to a maximum RMS relative error less than 0.03 per cent, the SEMI method is about 700 times faster than the direct solution.

Key words: cylindrical system of vector functions, elastic isotropy, fast algorithm, multilayered structure, propagator matrix method, surface Green's function.

1 INTRODUCTION

The problem of determining the elastic response of a half-space subject to surface loads was introduced by Boussinesq in 1885 and since then it has attracted the attention of many illustrious mathematicians, physicists and engineers—see Love (1944) for a discussion of the early literature. Later workers extended the original problem so as to address specific loading geometries, non-uniformity or anisotropy of the elastic medium, and the loading response of plates and shells as well as half-spaces, and these solutions have been applied in areas as diverse as cell biology (e.g. Balaban *et al*. 2001), civil engineering (e.g. Graig 1997) and earth science (e.g. Bevis *et al*. 2004; Becker & Bevis 2004). One of the most important extensions of the Boussinesq problem addresses the loading response of a layered elastic half-space—see Pan (1997) for a brief review of the methods proposed to date. Layered elastic structures are ubiquitous: superlattices in solid-state physics (Bimberg

et al. 1999), composites in material science (Agarwal & Broutman 1980; Schwarzer 2000), earth or foundation structures (Murthy 2003) and layered pavements for highway transportation (Khazanovich 1994; Brill & Hayhoe 2004). Modern analytical and numerical research into the loading of layered elastic structures addresses both forward and inverse problems (Yue & Yin 1998; Wang *et al*. 2003; Pan & Han 2005). To the best of the authors' knowledge, however, even for the relatively simple forward class of problems, no existing algorithms are fast enough to allow the loading response to be computed at (or even approaching) the interactive time scale.

In this paper we develop a new approach to computing the surface response of a layered elastic half-space to surface pressure loading. We assume that the pressure (i.e. normal stress) field is applied only within a finite surface area (e.g. within a given polygon) but otherwise is arbitrary. The arbitrary surface pressure field is discretized using a large number, n, of equally sized circular loading elements, and the pressure imposed in each element is uniform within each circle. The problem is to compute the displacement at a large number, m, of points (or stations) distributed over the surface. Because (1) the elastic response to a uniform circular loading element is axisymmetric, and both the radial and the vertical displacements at the surface depend only on the distance between the centre of the load and the point where displacement is being computed and (2) the displacement field produced by a single circular load scales linearly with the pressure imposed within that circle, we can transform our original problem into a nearly equivalent problem: computing the surface deformation field caused by a single unit pressure load at a total of $m\,n$ stations (where $m\,n$ is the product $m \times n$). We shall discuss this transformation at greater length elsewhere (Bevis *et al*. 2007). The solution of the original problem can be obtained from the solution of the parallel problem at very little additional computational cost. In order to exploit this framework, we must be able to compute the surface response at a huge number of points or stations.

This paper is focused on the key task of developing an extremely fast algorithm for calculating the surface displacements due to a uniform circular pressure load on the surface of the layered isotropic elastic half-space. To achieve our goal, we first express the displacement solution in terms of a cylindrical system of vector functions (involving infinite integrals of Bessel functions) and the propagator matrix method (Gilbert & Backus 1966; Pan 1989a,b, Pan 1997). We employ adaptive Gauss quadrature (e.g. Lucas 1995) to carry out the infinite integration where the zeros in the integrands are predicted and an acceleration method is introduced to speed up the integration. Even though the adaptive Gauss quadrature is very accurate and efficient as compared to the simple Simpson or trapezoidal integrations, point-by-point calculation is still extremely CPU intensive. To solve the speed problem, we propose a novel two-stage algorithm, namely the sparse evaluation and massive interpolation (SEMI) method.

During the first stage (sparse evaluation) we compute a high accuracy solution to the loading problem at a relatively small number of points using the direct (expensive) method mentioned above. The elementary loading problem is axisymmetric and so its solution can be stated in terms of radial and vertical components of displacement, both of which are scalar functions of the radial coordinate r, where $r = 0$ corresponds to the centre of the circular load. The small number (M) of r-values where we directly evaluate the solution are referred to as control points or knots. In the second stage (massive interpolation) we produce an approximate estimate of the displacement at any number of points (r-values) by interpolating between the values determined at the control points. To do this we divide the surface domain ($r = 0$ to infinity) into three sections and utilize a specific interpolation method based on the morphology or character of the surface displacement field in each section.

We have engaged in a series of numerical experiments to determine the accuracy and the speed of the SEMI approach as compared to direct evaluation. To compute the loading response at a large number of points, say 100 000 stations, with a modest degree of error, say with maximum RMS relative error of less than 0.2 per cent, our SEMI method is ∼1200 times faster than direct point-by-point evaluation. For more accurate results with maximum RMS relative error of less than 0.03 per cent, our SEMI method is still ∼700 times faster than the direct calculation.

This paper is organized as follows: In Section 2, we state the problem and the governing equations. In Section 3, the general solutions of the field quantities are derived using propagator matrices and the cylindrical system of vector functions. The special solution for the case of the uniform circular load is discussed in detail in Section 4. Section 5 presents the SEMI method outlined above. In Section 6, Numerical examples are provided to assess accuracy and computational efficiency (and interesting features in our SEMI approach are identified), and finally we discuss our results in Section 7.

2 PROBLEM STATEMENT AND GOVERNING EQUATIONS

Let us consider a layered half-space made up of p parallel, elastic isotropic layers lying over an elastic isotropic half-space. The layers are numbered serially with the layer at the top being layer 1 and the last layer p, which is just above the half-space (Fig. 1). We place the cylindrical coordinate on the surface with the z-axis pointing into the layered half-space. The kth layer is bounded by the interfaces $z = z_{k-1}$, z_k. As such, z_{k-1} is the coordinate of the upper interface of the kth layer, and z_k that of the lower interface. It is obvious that the thickness of the kth layer is $h_k = z_k - z_{k-1}$, with $z_0 = 0$ and $z_p = H$, where H is the depth of the last layer interface. The interfaces between the adjacent layers are assumed to be welded. The top surface is subject to uniform unit pressure within a circle of radius R. For a well-posed problem, the solution in the homogeneous half-space of the layered system should be also finite when the physical dimension approaches infinity.

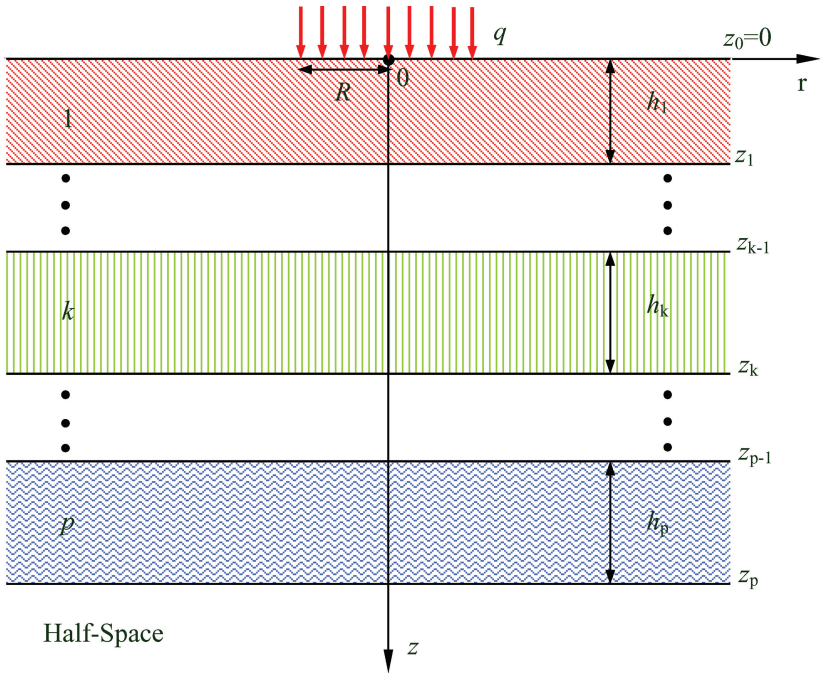

Figure 1. A multilayered elastic half-space under uniform vertical load q within the circle of radius R.

For the isotropic elastic solid, we have, in each layer, the following governing equations in the cylindrical coordinates:

(1) Equilibrium equations without body force:

$$\begin{aligned}
&\frac{\partial \sigma_{rr}}{\partial r}+\frac{\partial \sigma_{r\theta}}{r\partial \theta}+\frac{\partial \sigma_{rz}}{\partial z}+\frac{\sigma_{rr}-\sigma_{\theta\theta}}{r}=0\\
&\frac{\partial \sigma_{r\theta}}{\partial r}+\frac{\partial \sigma_{\theta\theta}}{r\partial \theta}+\frac{\partial \sigma_{\theta z}}{\partial z}+\frac{2\sigma_{r\theta}}{r}=0\\
&\frac{\partial \sigma_{rz}}{\partial r}+\frac{\partial \sigma_{\theta z}}{r\partial \theta}+\frac{\partial \sigma_{zz}}{\partial z}+\frac{\sigma_{rz}}{r}=0
\end{aligned}, \tag{1}$$

where σ_{ij} is the stress tensor.

(2) Constitutive relations:

$$\begin{aligned}
\sigma_{rr}&=c_{11}\gamma_{rr}+c_{12}(\gamma_{\theta\theta}+\gamma_{zz})\\
\sigma_{\theta z}&=c_{44}\gamma_{\theta z}
\end{aligned}, \tag{2}$$

where

$$c_{11}=\frac{E(1-\nu)}{(1+\nu)(1-2\nu)};\quad c_{12}=\frac{E\nu}{(1+\nu)(1-2\nu)};\quad c_{44}=\frac{E}{2(1+\nu)}. \tag{3}$$

The constitutive relations for the other normal and shear components can be found similarly. While in eq. (2), γ_{ij} are the engineering strain components, in eq. (3), E and ν are, respectively, Young's modulus and Poisson's ratio.

(3) The strain–displacement relations:

$$\begin{aligned}
&\gamma_{rr}=\frac{\partial u_r}{\partial r},\quad \gamma_{\theta\theta}=\frac{\partial u_\theta}{r\partial\theta}+\frac{u_r}{r},\quad \gamma_{zz}=\frac{\partial u_z}{\partial z}\\
&\gamma_{\theta z}=\frac{\partial u_\theta}{\partial z}+\frac{\partial u_z}{r\partial\theta},\quad \gamma_{rz}=\frac{\partial u_z}{\partial r}+\frac{\partial u_r}{\partial z},\quad \gamma_{r\theta}=\frac{\partial u_r}{r\partial\theta}+\frac{\partial u_\theta}{\partial r}-\frac{u_\theta}{r}
\end{aligned}, \tag{4}$$

where u_i is the displacement field.

3 GENERAL SOLUTION IN TERMS OF CYLINDRICAL SYSTEM OF VECTOR FUNCTIONS

The cylindrical system of vector functions is very convenient in treating axisymmetric problem and it is defined as (Pan 1989a,b, 1997)

$$\begin{aligned}
\mathbf{L}(r,\theta;\lambda,m)&=\mathbf{e}_z S(r,\theta;\lambda,m),\\
\mathbf{M}(r,\theta;\lambda,m)&=\left(\mathbf{e}_r\frac{\partial}{\partial r}+\mathbf{e}_\theta\frac{\partial}{r\partial\theta}\right)S(r,\theta;\lambda,m),\\
\mathbf{N}(r,\theta;\lambda,m)&=\left(\mathbf{e}_r\frac{\partial}{r\partial\theta}-\mathbf{e}_\theta\frac{\partial}{\partial r}\right)S(r,\theta;\lambda,m)
\end{aligned} \tag{5}$$

with

$$S(r,\theta;\lambda,m)=\frac{1}{\sqrt{2\pi}}J_m(\lambda r)e^{im\theta}, \tag{6}$$

where $J_{\rm m}(\lambda r)$ is the Bessel function of order m with $m=0$ corresponding to the axisymmetric deformation, which will be discussed in detail later on. It should be also noticed that the scalar function S in eq. (6) satisfies the Helmholtz equation

$$\frac{\partial^2 S}{\partial r^2}+\frac{\partial S}{r\partial r}+\frac{\partial^2 S}{r^2\partial\theta^2}+\lambda^2 S=0. \tag{7}$$

We quickly remark that the cylindrical system of vector functions is an extension of the Hankel transform and can be directly applied to a vector function. Since this vector function system (eq. 5) forms an orthogonal and complete space, any integrable vector and/or scalar function can be expressed in terms of it. In particular, the displacement and traction (with the z-axis as the normal) vectors can be expressed as

$$\mathbf{u}(r,\theta,z)=\sum_m\int_0^{+\infty}[U_L(z)\mathbf{L}(r,\theta)+U_M(z)\mathbf{M}(r,\theta)+U_N(z)\mathbf{N}(r,\theta)]\lambda{\rm d}\lambda \tag{8}$$

$$\begin{aligned}\mathbf{t}(r,\theta,z)&\equiv\sigma_{rz}\mathbf{e}_r+\sigma_{\theta z}\mathbf{e}_\theta+\sigma_{zz}\mathbf{e}_z\\&=\sum_m\int_0^{+\infty}[T_L(z)\mathbf{L}(r,\theta)+T_M(z)\mathbf{M}(r,\theta)+T_N(z)\mathbf{N}(r,\theta)]\lambda{\rm d}\lambda.\end{aligned} \tag{9}$$

Making use of these expansions along with the strain–displacement and constitutive relations, we have, in general,

$$u_r(r,\theta,z)=\sum_m\int_0^{\infty}\left(U_M\frac{\partial S}{\partial r}+U_N\frac{\partial S}{r\partial\theta}\right)\lambda{\rm d}\lambda \tag{10a}$$

$$u_\theta(r,\theta,z)=\sum_m\int_0^{\infty}\left(U_M\frac{\partial S}{r\partial\theta}-U_N\frac{\partial S}{\partial r}\right)\lambda{\rm d}\lambda \tag{10b}$$

$$u_z(r,\theta,z)=\sum_m\int_0^{\infty}U_L S\lambda{\rm d}\lambda \tag{10c}$$

$$\sigma_{rr}(r,\theta,z)=\sum_m\int_0^{\infty}\left[c_{11}\left(U_M\frac{\partial^2 S}{\partial r^2}+U_N\frac{\partial^2 S}{r\partial r\partial\theta}-U_N\frac{\partial S}{r^2\partial\theta}\right)+c_{12}\left(U_M\frac{\partial^2 S}{r^2\partial\theta^2}+U_M\frac{\partial S}{r\partial r}-U_N\frac{\partial^2 S}{r\partial r\partial\theta}+U_N\frac{\partial S}{r^2\partial\theta}\right)+c_{12}\frac{{\rm d}U_L}{{\rm d}z}S\right]\lambda{\rm d}\lambda \tag{11a}$$

$$\sigma_{\theta\theta}(r,\theta,z)=\sum_m\int_0^{\infty}\left[c_{12}\left(U_M\frac{\partial^2 S}{\partial r^2}+U_N\frac{\partial^2 S}{r\partial r\partial\theta}-U_N\frac{\partial S}{r^2\partial\theta}\right)+c_{11}\left(U_M\frac{\partial^2 S}{r^2\partial\theta^2}+U_M\frac{\partial S}{r\partial r}-U_N\frac{\partial^2 S}{r\partial r\partial\theta}+U_N\frac{\partial S}{r^2\partial\theta}\right)+c_{12}\frac{{\rm d}U_L}{{\rm d}z}S\right]\lambda{\rm d}\lambda \tag{11b}$$

$$\sigma_{zz}(r,\theta,z)=\sum_m\int_0^{\infty}\left(-\lambda^2 c_{12}U_M+c_{11}\frac{{\rm d}U_L}{{\rm d}z}\right)S\lambda{\rm d}\lambda \tag{11c}$$

$$\sigma_{\theta z}(r,\theta,z)=c_{44}\sum_m\int_0^{\infty}\left(\frac{{\rm d}U_M}{{\rm d}z}\frac{\partial S}{r\partial\theta}-\frac{{\rm d}U_N}{{\rm d}z}\frac{\partial S}{\partial r}+\frac{1}{r}U_L\frac{\partial S}{\partial\theta}\right)\lambda{\rm d}\lambda \tag{11d}$$

$$\sigma_{rz}(r,\theta,z)=c_{44}\sum_m\int_0^{\infty}\left(\frac{{\rm d}U_M}{{\rm d}z}\frac{\partial S}{\partial r}+\frac{{\rm d}U_N}{{\rm d}z}\frac{\partial S}{r\partial\theta}+U_L\frac{\partial S}{\partial r}\right)\lambda{\rm d}\lambda \tag{11e}$$

$$\sigma_{r\theta}(r,\theta,z)=c_{44}\sum_m\int_0^{\infty}\left[U_M\left(\frac{2\partial^2 S}{r\partial r\partial\theta}-\frac{2\partial S}{r^2\partial\theta}\right)+U_N\left(\frac{\partial^2 S}{r^2\partial\theta^2}-\frac{\partial^2 S}{\partial r^2}+\frac{\partial S}{r\partial r}\right)\right]\lambda{\rm d}\lambda. \tag{11f}$$

The relation of the expansion coefficients between $T_{\rm I}$ and $U_{\rm I}$ (I = L, M, N) can be found by comparing eqs (9) to (11c–e)

$$T_L=-\lambda^2 c_{12}U_M+c_{11}\frac{{\rm d}U_L}{{\rm d}z}, \tag{12a}$$

$$T_M=c_{44}\left(U_L+\frac{{\rm d}U_M}{{\rm d}z}\right), \tag{12b}$$

$$T_N=c_{44}\frac{{\rm d}U_N}{{\rm d}z}. \tag{12c}$$

Substituting the stress expansion (11) into the equilibrium eq. (1), we further find

$$\frac{{\rm d}T_L}{{\rm d}z}-\lambda^2 T_M=0, \tag{13a}$$

$$-\lambda^2 c_{11} U_M + c_{12}\frac{\mathrm{d}U_L}{\mathrm{d}z} + \frac{\mathrm{d}T_M}{\mathrm{d}z} = 0, \tag{13b}$$

$$\frac{\mathrm{d}T_N}{\mathrm{d}z} - \lambda^2 c_{44} U_N = \phi. \tag{13c}$$

Noticing that the ***N***-type solution is dependent to the **L&M**-type solution, we introduce the following two sets of coefficient vectors

$$[\mathbf{E}] = [U_L, \lambda U_M, T_L/\lambda, T_M]^t \tag{14a}$$

$$[\mathbf{E}^N(z)] = [U_N(z), T_N(z)/\lambda]^t \tag{14b}$$

then the homogeneous solution in each layer from eqs (12) and (13) are found to be

$$[\mathbf{E}(z)] = [\mathbf{Z}(z)][\mathbf{K}] \tag{15a}$$

$$[\mathbf{E}^N] = [\mathbf{Z}^N(z)][\mathbf{K}^N], \tag{15b}$$

where $[\boldsymbol{K}]$ and $[\boldsymbol{K}^N]$ are column coefficient vectors of 4×1 and 2×1, respectively, with their elements to be determined by the interface and/or boundary conditions. The matrices $[\boldsymbol{Z}(z)]$ and $[\boldsymbol{Z}^N(z)]$ are the solution matrices given in Appendix A.

The propagating relations for the coefficient vectors $[\boldsymbol{E}]$ and $[\boldsymbol{E}^N]$ of kth layer at the z-level z_{k-1} and that at z_k, are found to be

$$[\mathbf{E}(z_{k-1})] = [\mathbf{a}_k][\mathbf{E}(z_k)], \tag{16a}$$

$$\left[\mathbf{E}^N(z_{k-1})\right] = \left[\mathbf{a}_k^N\right]\left[\mathbf{E}^N(z_k)\right], \tag{16b}$$

where $[\boldsymbol{a}_k]$ and $[\boldsymbol{a}_k^N]$ are the propagator matrices for the kth layer, with their elements given in Appendix A.

4 SOLUTION FOR CIRCULAR SURFACE LOADING

Assume that a uniform vertical surface load of magnitude q is applied within the circle of $r = R$ (Fig. 1), then the traction boundary condition on the surface $z = 0$ is expressed as:

$$\sigma_{zz} = \begin{cases} -q & \mathrm{r} < \mathrm{R} \\ 0 & \mathrm{r} > \mathrm{R} \end{cases} . \tag{17}$$

$$\sigma_{rz} = \sigma_{\theta z} = 0\, 0 \le r < \infty$$

Therefore, the corresponding expansion coefficients in the cylindrical system of vector functions are:

$$T_L(\lambda, 0) = -\frac{q R\sqrt{2\pi}}{\lambda} J_1(\lambda R). \tag{18}$$

$$T_M(\lambda, 0) = T_N(\lambda, 0) = 0$$

It is clear that the solution to the ***N***-type is identically zero and therefore we need to solve the **L&M**-type problem (axisymmetric) only. We now first solve the problem in the transformed domain (i.e. in terms of the expansion coefficients). Propagating the propagator matrix $[\boldsymbol{a}_k]$ from the top of the homogeneous half-space $z = H$ to the surface $z = 0$, we find

$$[\mathbf{E}(0)] = [\mathbf{G}][\mathbf{K}_p], \tag{19}$$

where

$$[\mathbf{G}] = [\mathbf{a}_1][\mathbf{a}_2] - - - [\mathbf{a}_p][\mathbf{Z}_p(\mathbf{H})]. \tag{20}$$

The unknown coefficients $[\boldsymbol{K}_p]$ are those in the half-space. As the solution in the half-space should be bounded, the first and third elements in $[\boldsymbol{K}_p]$ should be zero (see Appendix A for the general solution in each layer). The remaining two unknown coefficients can be determined by the two boundary conditions on the surface $z = 0$ as given by eq. (18) (for the L- and M-components only).

After the unknown coefficients in $[\boldsymbol{K}_p]$ are determined, the expansion coefficients at any depth (e.g. in the kth layer with $z_{k-1} \le z \le z_k$) can be obtained exactly as:

$$[\mathbf{E}(z)] = [\mathbf{a}_k(z - z_{k-1})][\mathbf{a}_{k+1}] - - - [\mathbf{a}_p][\mathbf{Z}_p(\mathbf{H})][\mathbf{K}_p]. \tag{21}$$

In general, direct multiplication of the propagator matrix $[\boldsymbol{a}_k]$ can be carried out in order to propagate the transformed domain solution from one layer to the next. However, as discussed in Pan (1997), Yue & Yin (1998), and more recently by Fukahata & Matsu'ura (2005), overflow may occur from multiplication of matrices in eqs (20) and (21). Fortunately, this can be overcome by factoring out the exponentially growing factor in the elements of the propagator matrix. The resulting modified propagator matrices have no element growing exponentially, and therefore there will be no overflow problem for a multilayered half-space having any number of layers (no matter what the thickness of each layer).

After solving the problem in the transformed domain, the displacement and stress solutions at any location in the physical domain can be expressed (independent of θ because of symmetry) as:

$$u_r(r, z) = -\frac{1}{\sqrt{2\pi}} \int_0^\infty (\lambda U_M) J_1(\lambda r) \lambda \mathrm{d}\lambda \tag{22a}$$

$$u_\theta(r,z)=0 \tag{22b}$$

$$u_z(r,z)=\frac{1}{\sqrt{2\pi}}\int_0^\infty (U_L)J_0(\lambda r)\lambda \mathrm{d}\lambda \tag{22c}$$

$$\sigma_{rz}(r,z)=-\frac{1}{\sqrt{2\pi}}\int_0^\infty (T_M)J_1(\lambda r)\lambda^2 \mathrm{d}\lambda \tag{23a}$$

$$\sigma_{\theta z}(r,z)=\sigma_{r\theta}(r,z)=0 \tag{23b}$$

$$\sigma_{zz}(r,z)=\frac{1}{\sqrt{2\pi}}\int_0^\infty \left(\frac{T_L}{\lambda}\right)J_0(\lambda r)\lambda^2 \mathrm{d}\lambda \tag{23c}$$

$$\sigma_{rr}(r,z)=\frac{\nu}{1-\nu}\sigma_{zz}+\frac{2c_{44}}{\sqrt{2\pi}}\int_0^\infty (\lambda U_M)\left[-\frac{1}{1-\nu}J_0(\lambda r)\lambda+\frac{J_1(\lambda r)}{r}\right]\lambda \mathrm{d}\lambda \tag{23d}$$

$$\sigma_{\theta\theta}(r,z)=\frac{2\nu}{1-\nu}\sigma_{zz}-\sigma_{rr}-\frac{1}{\sqrt{2\pi}}\frac{E}{(1-\nu)}\int_0^\infty (\lambda U_M)J_0(\lambda r)\lambda^2 \mathrm{d}\lambda, \tag{23e}$$

where the expansion coefficients are functions of z and the transform variable λ.

Of particular interest is the displacement field on the surface, which, in geophysical context is often directly observable using GPS (Bevis *et al*. 2004) or InSAR. For a uniform circular load, the horizontal (radial) and vertical displacements on the surface can be expressed as:

$$u_r(r,0)=qR\int_0^\infty \frac{D_1}{\lambda}J_1(\lambda R)J_1(\lambda r)\mathrm{d}\lambda \tag{24a}$$

$$u_z(r,0)=-qR\int_0^\infty \frac{D_0}{\lambda}J_1(\lambda R)J_0(\lambda r)\mathrm{d}\lambda \tag{24b}$$

where

$$D_0=\frac{G_{12}G_{44}-G_{14}G_{42}}{G_{32}G_{44}-G_{34}G_{42}};\ D_1=\frac{G_{22}G_{44}-G_{24}G_{42}}{G_{32}G_{44}-G_{34}G_{42}} \tag{24c}$$

with G_{ij} being the elements of the matrix $[\boldsymbol{G}]$ in eq. (20). This matrix is a function of the transform variable λ, the elastic properties of the layered half-space, and the thickness of each layer.

To find the physical domain solutions, the transformed-domain results need to be integrated numerically. It is further noted that the integrands in the infinite integrals for the displacements involve products of Bessel functions that are oscillatory and go to zero slowly as their argument approaches infinity. Thus, the common numerical integration methods, such as the trapezoidal rule or Simpson's rule, are not suitable. While numerical integration of infinite integrals involving a single Bessel function has been discussed by Chave (1983) and Lucas & Stone (1995), the corresponding numerical integration involving products of Bessel functions of different orders has been studied by Lucas (1995) using adaptive Gaussian quadrature. We adopt this very accurate and efficient algorithm.

Base on this algorithm, the infinite integral is expressed as a summation of:

$$\int_0^{+\infty} f(\lambda)J_m(\lambda R)J_n(\lambda r)\mathrm{d}\lambda=\int_0^{r_{\max}} f(\lambda)J_m(\lambda R)J_n(\lambda r)\mathrm{d}\lambda+\int_{r_{\max}}^{+\infty} f(\lambda)J_m(\lambda R)J_n(\lambda r)\mathrm{d}\lambda \tag{25}$$

The finite and infinite integrations on the right-hand side of (25) are then calculated using the adaptive Gaussian quadrature (i.e. Chave 1983; Rice 1983). Furthermore, in applying the Gaussian quadrature, the mW transform and ε-algorithm are also introduced for handling the oscillation feature of the integrands and for accelerating the calculation (Lucas 1995; Lucas & Stone 1995). In the numerical analysis presented below, we have set the relative and absolute errors, respectively, at 10^{-4} and 10^{-5}.

5 SEMI ALGORITHM FOR SURFACE DISPLACEMENT FIELDS

As can be observed from eq. (24), for different surface locations (stations), the surface displacements need to be calculated one by one, which would involve substantial computation. This computational throughput problem motivates the development of the following SEMI algorithm.

Based on the form of the surface displacement components when considered as functions of r (as shown in Figs 2a,b and 3a,b for the two typical layered models given in Tables 1 and 2; many other layered models have been tested with all of them showing features similar to those seen in Figs 2 and 3), our SEMI algorithm divides the surface into three different sections: A near-field (from 0 to $2R$), a middle-field ($2R$ to $40R$), and a far-field ($40R$ to, say, $100R$) section. As can be observed from both Figs 2 and 3, in the near-field the displacement reaches the largest magnitude with the most severe changes in its slope and high-order derivatives occurring at the boundary of the circle. In the middle field, the variation of the displacement is very smooth and gentle. Finally in the far-field, the displacement asymptotically approaches zero. Therefore, in these different sections one should use different interpolation schemes. After many testing runs, we decided to employ the B-spline in physical domain for the near field, B-spline in nature logarithmic domain for the middle field, and the inverse ($1/r$) B-spline for the far-field. We discuss these separately below.

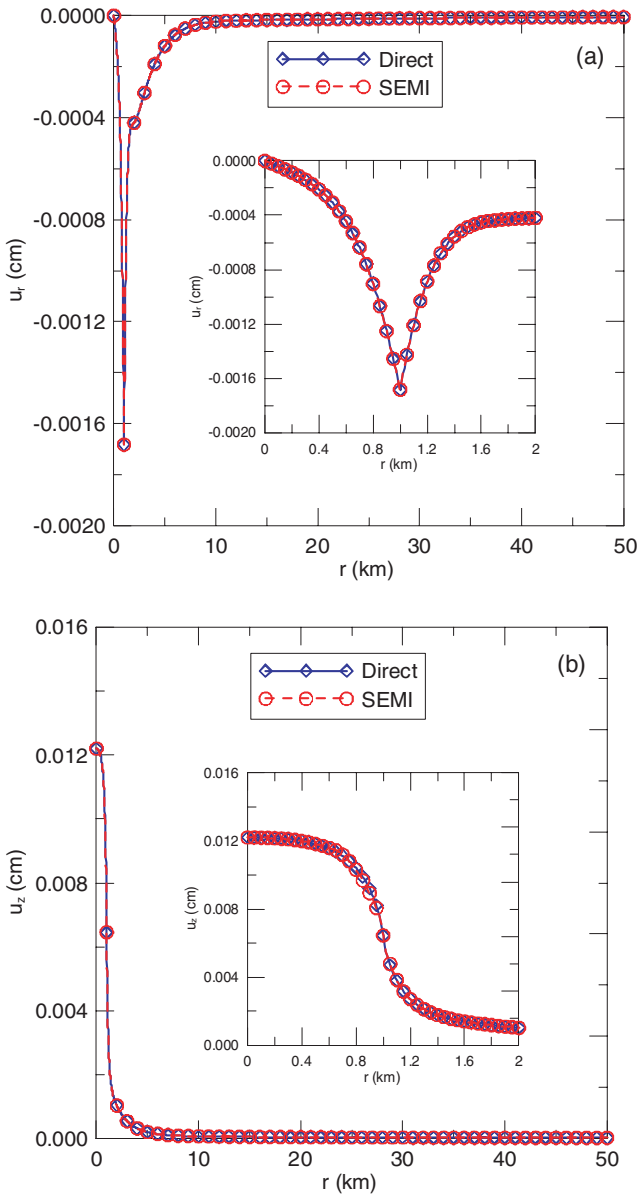

Figure 2. Comparison of the surface radial u_r (a) and vertical u_z (b) displacements for layered Model 1: Direct versus SEMI (based on Case II with 31 pre-calculation points).

5.1 Near- and middle-field pre-calculation with B-spline

Splines are piecewise polynomials of degree n joined together at control points with n-1 continuous derivatives. These control or break points of splines are often called knots. If $n \geq 2$, then the spline is smooth. In the B-spline algorithm, the targeted function, that is, $u(r)$, is expressed as (de Boor 1979; Rice 1983)

$$u(r) = \sum_{j=1}^{N} a_j B_j(r), \tag{26}$$

where $B_j = B_{j,k,t}$ denotes the jth B-spline of order k with respect to the knot sequence $\boldsymbol{t}$, and the coefficients a_j are solved from the following equation using the function values at data points r_i (i.e. requires that the B-spline passes exactly through each control point)

$$\sum_{j=1}^{N} a_j B_j(r_i) = u(r_i). \tag{27}$$

In B-spline, different orders using the knot sequence based upon the r-values of the data, that is, from order 2 (quadratic) through order 8, can be selected. In our algorithm, we fix the order at 3, and choose different number of control points to approximate both the near- and middle-fields.

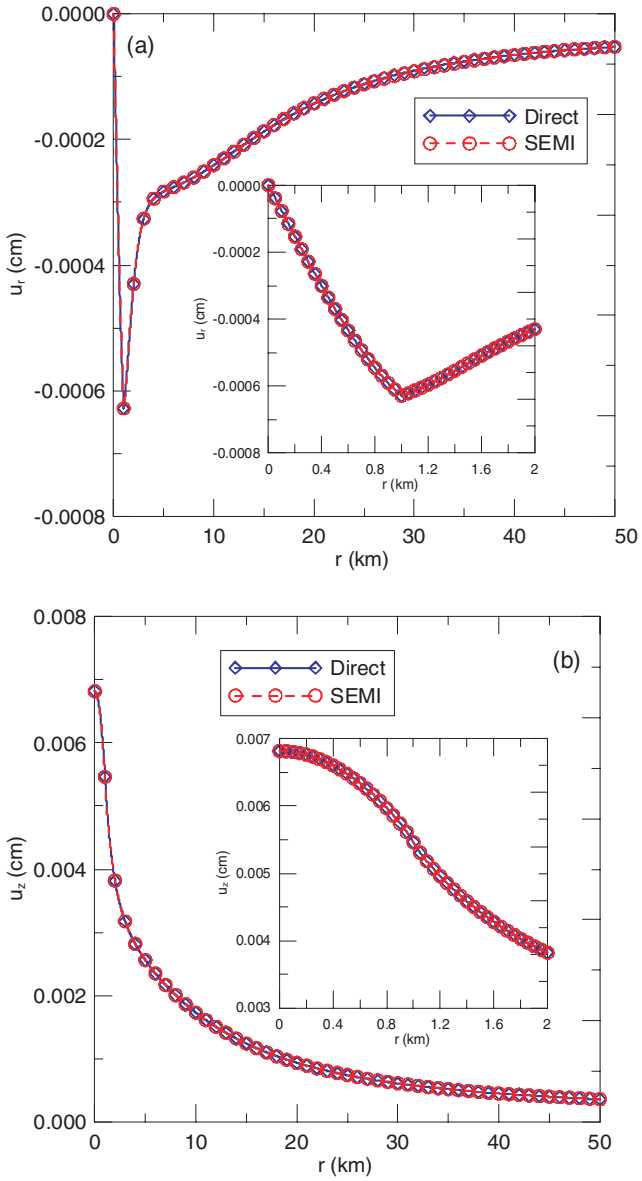

Figure 3. Comparison of the surface radial u_r (a) and vertical u_z (b) displacements for layered Model 2: Direct versus SEMI (based on Case II with 31 pre-calculation points).

Table 1. Layered Model 1: Pressure $q = 1$ kPa and loading radius $R = 1$ km

Layer no.	Thickness (km)	Young's modulus E (GPa)	Poisson's ratio ν
1	0.5	5.0	0.3
2	5	30.0	0.25
3	Infinite	150.0	0.2

Due to varying character of the surface displacement in the near- and middle-fields, different spline-based interpolation algorithms are developed in each sector. In the near field from 0 to $2R$, there is a well-known singular point in the surface stress at the edge of the circle $r = R$. Such a singularity corresponds to the sharp slope (and second order derivative) changes in displacements which cannot be easily treated even with the B-spline approximation. Therefore, we further separate the near field into three subsections: 0 to $R - \delta$, $R - \delta$ to $R + \delta$, and $R + \delta$ to $2R$. While the direct physical-domain B-spline is utilized to approximate the displacements in the first and third subsections, direct calculation with linear interpolation is proposed for the middle subsections. After numerous testing runs, we have selected the optimal $\delta = 0.03R$, whilst in the first and third B-spline domains graded distance is proposed to find the key point locations. For these two subsections, the graded distance is chosen to be $g = 1.5$ with increasing r_i, which means $|r_{i+1} - r_i| = 1.5|r_i - r_{i-1}|$.

Table 2. Layered Model 2: pressure $q = 1$ kPa and loading radius $R = 1$ km

Layer no.	Thickness (km)	Young's modulus E (GPa)	Poisson's ratio ν
1	0.5	150.0	0.2
2	5	30.0	0.25
3	Infinite	5.0	0.3

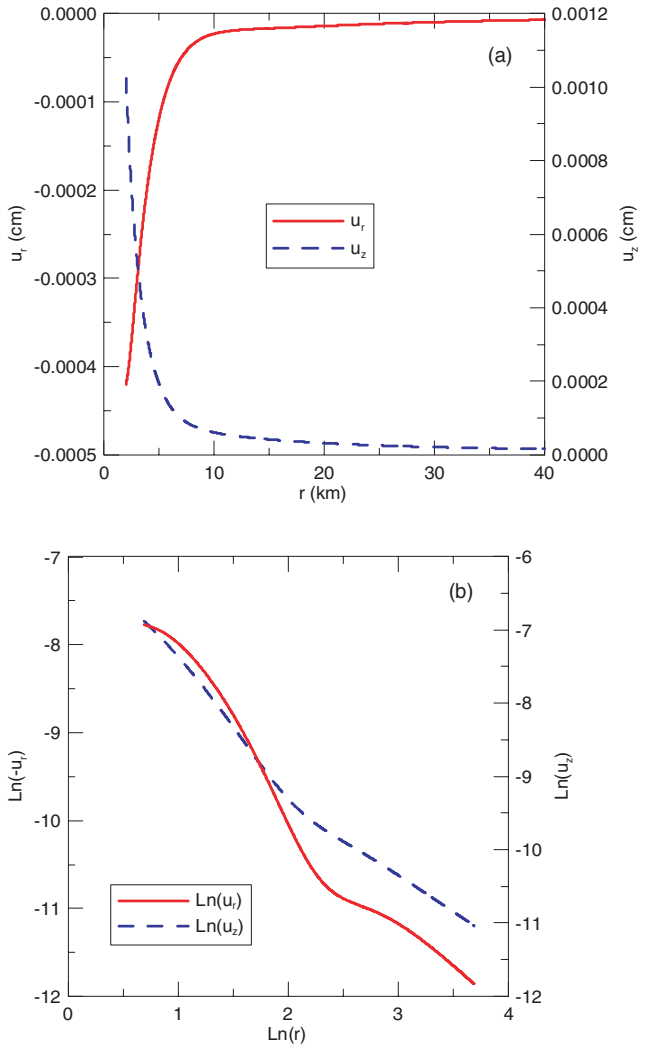

Figure 4. Variation of the surface radial and vertical displacements versus radial distance r for layered Model 1: In the physical domain (a) and in the nature Ln domain (b).

For the middle field from $2R$ to $40R$, we also employ the B-spline approximation. However, instead of using the B-spline in the physical domain directly, we use it in the nature logarithmic domain. Our B-spline interpolation scheme is based on the fact that the displacement response in the nature logarithmic domain is smoother than that in the physical domain. This can be observed in Figs 4(a) and (b) for the horizontal and vertical displacement distributions for Model 1 in the physical- (Fig. 4a) and nature Ln- (Fig. 4b) domains. Numerical experiments based on different layered half-space structures have also validated our decision to work in the nature Ln-domain. Furthermore, due to the smooth feature of the displacement in the nature Ln-domain, we use uniformly distributed control points in the Ln-domain [Ln(r)], unlike the scheme we use in the near-field case where graded distance is chosen with increasing r in the physical domain.

5.2 Far-field pre-calculation using inverse B-spline

For r larger than $40R$, the displacement field decays to zero, inversely proportional to the distance. Therefore, for a given circular load, the magnitude of the displacements in the far-field would be small or very small as compared to those in the near- and middle-fields. However, we can still include this far-field response from $r = 40R$ all the way, say to $r = 100R$ (if required, further extension to $r = 1000R$ or even $r = 5000R$ can be easily achieved by just adding a couple of more control points as for the $r = 100R$ case discussed below). In this section, we

Table 3. Number of points in different sectors (i.e. Cases I–IV) and the corresponding RMS relative errors (per cent) between the direct and SEMI methods for Model 1.

	Case I				Case II			
Sect	pts	RMS_{ur}	RMS_{uz}	RMS_{max}	pts	RMS_{ur}	RMS_{uz}	RMS_{max}
1	13	3.83	3.28	3.83	19	0.323	0.740	0.740
2	6	3.98	1.19	3.98	11	0.273	0.0779	0.273
3	3	0.0796	0.00154	0.0796	3	0.0796	0.00154	0.0796
Max	20	3.98	3.28	3.98	31	0.323	0.740	0.740
	Case III				Case IV			
Sect	pts	RMS_{ur}	RMS_{uz}	RMS_{max}	pts	RMS_{ur}	RMS_{uz}	RMS_{max}
1	31	0.0433	0.173	0.173	55	0.00597	0.00938	0.00938
2	21	0.0191	0.00613	0.0191	41	0.00208	0.00067	0.00208
3	4	0.0395	0.00115	0.0395	5	0.0216	0.00084	0.0216
Max	54	0.0433	0.173	0.173	99	0.0216	0.00938	0.0216

propose the following B-spline in terms of the inverse distance $x = 1/r$ for the displacement u (u_r and u_z) as

$$u(x) = \sum_{j=1}^{N} b_j B_j(x), \tag{28}$$

where the coefficients b_j are solved by using the function values at the predetermined control points x_i ($x_i = 1/r_i$) in the interval of $r = 40R-100R$, similar to (27). We remark that, for a couple of special examples where the far-field displacement decays monotonically, a simple asymptotical expansion may give slightly accurate results than the inverse B-spline. However, the inverse B-spline proposed here can be applied to the general case.

6 DIRECT VERSUS SEMI METHODS: NUMERICAL COMPARISON

In this section, two typical layered models listed in Tables 1 and 2 are selected to test our pre-calculation algorithm. While Model 1 corresponds to the earth structure, Model 2 is the inverse layup of the Model 1 material properties, which is a typical layered pavement structure. Furthermore, for each model, four different cases with different number of key points (Case I with 20 points, Case II with 31 points, Case III with 54 points, and Case IV with 99 points) are studied (Table 3).

First, shown in Figs 2 and 3 are the comparison of the surface displacements based on both the direct and SEMI methods for both models 1 and 2 with 31 pre-calculation points for SEMI (i.e. Case II), with station points vary from 0 to $50R$ at an increment of $0.1R$. The inserted figures are the zoom-in results from 0 to $2R$ to show the rapid variation of the displacement fields in the near field. As can be observed from these figures, our SEMI results agree well with those calculated directly.

Secondly, to quantitatively evaluate the accuracy of the proposed SEMI algorithm, we have also estimated relative errors (Figs 5 and 6) and the RMS relative errors (Table 3) between the direct and SEMI approaches. Listed in Table 3 are the SEMI results as compared to the direct calculation for Model 1 from $r = 0$ to $r = 100R$ for the four Cases I to IV in terms of the RMS relative errors. In this table, 'Sect' stands for the three different sections (1 for near-field, 2 for middle-field, and 3 for far-field); 'Max' stands for the total number of control points (pts in the table) used in the SEMI approach; RMS_{ur} and RMS_{uz} are the RMS relative errors in the radial and vertical displacements as compared to the direct results, with the maximum between these two being RMS_{max}. For these four sets of control points (corresponding to Cases I–IV), we have further plotted the detailed relative errors between the SEMI and the direct methods as the function of r, as presented in Figs 5(a) and (b) for the radial and vertical displacements for Model 1 and in Figs 6(a) and (b) for Model 2. Figs 5 and 6 show clearly that as the number of control points increases the relative errors in the SEMI solutions decline rapidly.

Thirdly, we have also studied the decay behaviour of the RMS relative error in displacements as a function of the number M of control points. The RMS relative error is determined by comparing the approximate solutions obtained using the SEMI method with those obtained (far more slowly) via direct evaluation (i.e. the same approach used to compute the displacements at the M control points). The rapid decay trend can be observed in Table 3 for the maximum RMS relative errors and can even be expressed approximately in proportion to $1/M^n$, with n being larger than 3 for the whole domain from 0 to 100R. Such a fast decay feature is also shown in Fig. 7 where the RMS relative errors in the displacements u_r and u_z for Model 1 as a function of the total number M, along with their corresponding fitting curves are plotted. The fitted curves for the RMS relative u_r and u_z are, respectively, $27\,762/M^{3.1867}$ and $11\,6561/M^{3.4912}$.

Finally, for fixed RMS relative errors (i.e. Cases I–IV), we have compared the CPU times based on both the direct and SEMI methods. Listed in Table 4 are the CPU times for the two layered models for four values of M. As can be observed, our SEMI is much faster than the direct method, in particular when the station number is very large. More specifically, for 500 surface stations, our SEMI algorithm is about 25 times faster than the direct method, and for 100 000 points, our algorithm is at least 1200 times faster than the direct method (when M is 54). Furthermore, there is virtually no difference in CPU time based on the SEMI approach when the number of the control points increases from 20 (Case I corresponding to $RMS_{max} \leq 4$ per cent) to 54 (Case III corresponding to $RMS_{max} \leq 0.2$ per cent). Even for Case IV which

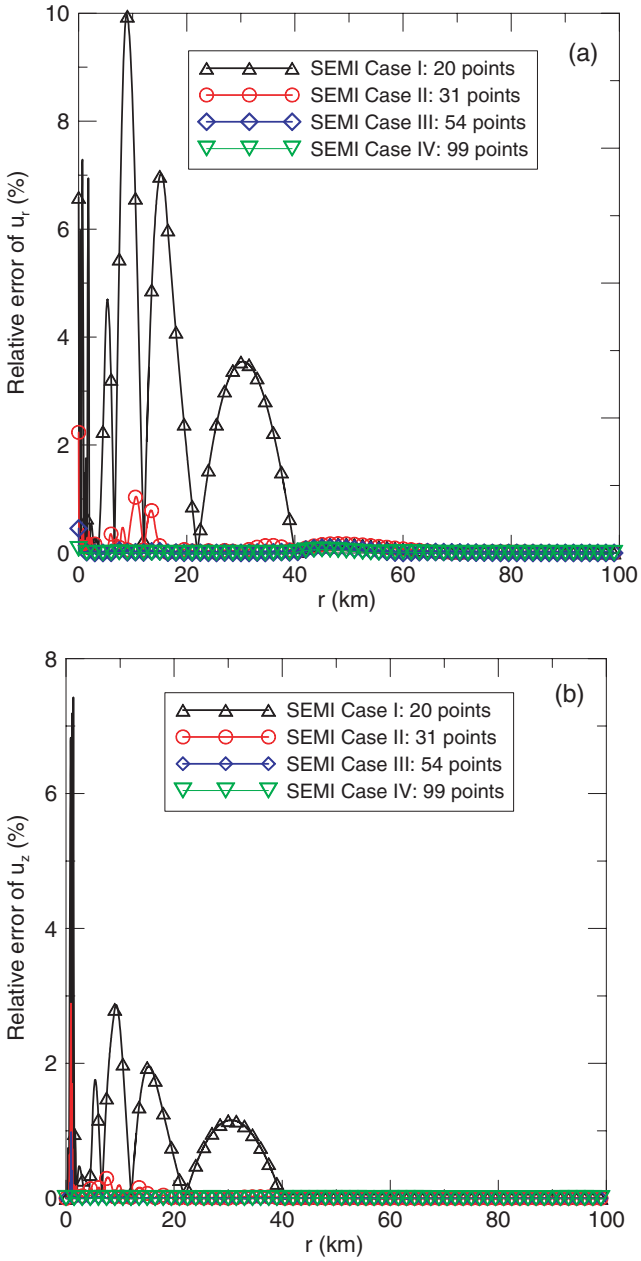

Figure 5. Relative errors in surface displacements u_r (a) and u_z (b) for Model 1 for the four SEMI Cases with different number of pre-calculation points.

corresponds to the more accurate result (i.e. $\mathrm{RMS}_{\max} \leq 0.03$ per cent) with $M = 99$, our SEMI is still about 700 times faster than the direct method.

7 DISCUSSION

We have developed a rapid numerical method for the calculation of surface displacement fields due to a uniform circular loading on the surface of the layered Cartesian half-space. High accuracy solutions can be obtained by combining a cylindrical system of vector functions with the propagator matrix method. Instead of evaluating these solutions at every station of interest, which would be computationally expensive due to the presence of slowly converging integrals, we perform these calculations only at a limited number of control points, and then estimate the displacements at intervening points via interpolation. By varying the number of control points used, one can trade off computational speed and numerical accuracy according to the needs of the application. In another paper (Bevis *et al*., in preparation, 2007) we will provide a variety of examples that illustrate how the SEMI method provides a practical basis for calculating the surface response due to any spatial distribution of surface loading by approximating the laterally varying load using large numbers of circular loading elements.

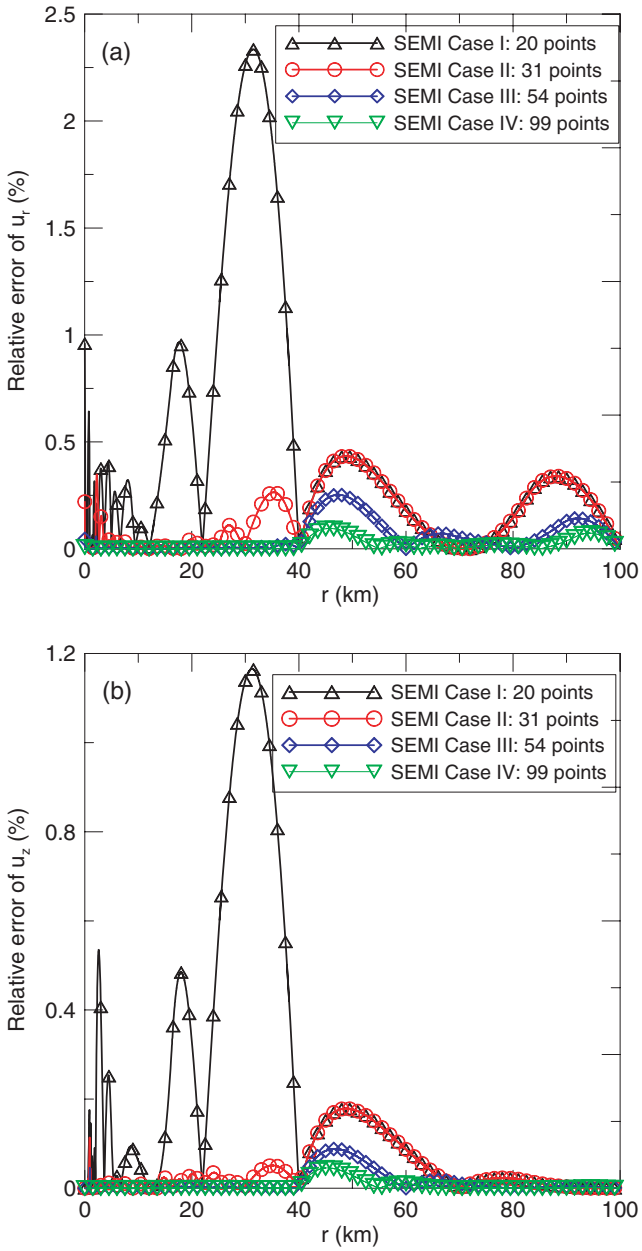

Figure 6. Relative errors in surface displacements u_r (a) and u_z (b) for Model 2 for the four SEMI Cases with different number of pre-calculation points.

There are probably many ways in which the second (interpolation) stage of the SEMI method can be realized, and we presented only one such strategy in this paper, though it is a composite strategy. The surface, that is, the *r*-axis, is divided into three sections (near-, middle-, and far-fields) with certain number of pre-selected control points in each section. Due to the different character of the displacement function in these sections, three different approaches have been developed for interpolating between the control points. For a half-space composed of two-layers over a uniform half-space, computing the loading response at 100 000 different surface locations is achieved more than 1200 time faster if we use the SEMI approach rather than the direct method, and the RMS relative error in displacement is everywhere less than 0.2 per cent. For maximum RMS relative error less than 0.03 per cent, our SEMI approach is still about 700 times faster than the direct method.

While detailed applications of the SEMI approach to any polygonal load is discussed in a future paper, we remark that our SEMI algorithm has also been verified and validated by other direct codes for layered elastic half-spaces. For instance (Han 2006), for a uniform load over a rectangle of 1000 m × 2000 m which is over a three-layered half-space, we calculated the displacements along different lines on the surface using our SEMI with 20 × 40 circular elements and compared the results with those by Yue & Xiao (2005, private communication) using the direct numerical integration formulation. It is found that the RMS relative error of all the surface displacements between the SEMI and Yue & Xiao is at most 4 per cent. Furthermore, this error can be reduced if more circular elements are used (Han 2006).

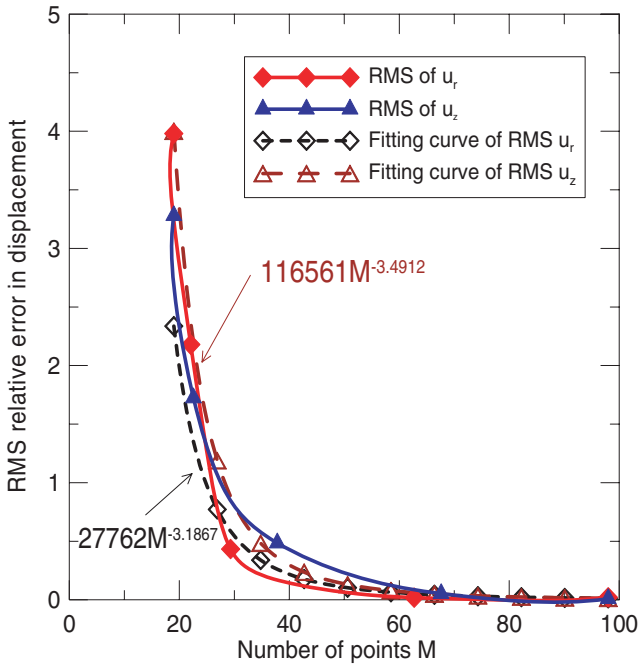

Figure 7. RMS relative errors of surface displacements u_r and u_z versus number of pre-calculation points for Model 1.

Table 4. Comparison of CPU times between direct and SEMI methods.

			500 points	1000 points	10 000 points	100 000 points
Model 1	Direct		24s	48s	8m6s	80m37s
	SEMI	I	<1s	<1s	1s	3s
		II	<1s	<1s	1s	3s
		III	<2s	<2s	2s	4s
		IV	<4s	<4s	4s	7s
Model 2	Direct		25s	51s	8m32s	84m37s
	SEMI	I	<1s	<1s	1s	3s
		II	<1s	1s	2s	3s
		III	<2s	2s	3s	4s
		IV	<4s	4s	5s	7s

Computer configuration: Dell Workstation PWS650, Xeon CPU 3.06 GHz, 2.0GB RAM.

ACKNOWLEDGMENT

The authors would like to thank Professors Z. Q. Yue and H. T. Xiao from University of Hong Kong for discussion on the direct calculation of surface responses in layered structures and for verification on our SEMI program. MB and HZ were supported by NASA contract NNG04GF28G, and EP, FH and RZ partially by the Ohio DOT.

REFERENCES

Agarwal, B.D. & Broutman, L.J., 1980. *Analysis and Performance of Fiber Composites,* John Wiley & Sons, New York.

Balaban, N.Q. *et al.*, 2001. Force and focal adhesion assembly: a close relationship studied using elastic micropatterned substrates, *Nat. Cell Biol.,* **3,** 466–472.

Becker, J.M. & Bevis, M., 2004. Love's problem, *Geophys. J. Int.,* **156,** 171–178.

Bevis, M., Kendrick, E., Cser, A. & Smalley, R., 2004. Geodetic measurement of the local elastic response to the changing mass of water in Lago Laja, Chile, *Phys. Earth Planet. Inter.,* **141,** 71–78.

Bimberg, D., Grundmann, M. & Ledentsov, N.N., 1999. *Quantum Dot Heterostructures,* John Wiley & Sons, New York.

Brill, D.R. & Hayhoe, G.F., 2004. Multiple-gear analysis for flexible pavement design in LEDFAA, *FAA Worldwide Airport Technology Transfer Conference,* Atlantic City, New Jersey, pp. 1–10.

Chave, A.D., 1983. Numerical integration of related Hankel transforms by quadrature and continued fraction expansion, *Geophysics,* **48,** 1671–1686.

de Boor, C.R., 1979. *A Practical Guide to Splines,* Springer-Verlag, New York.

Fukahata, Y. & Matsu'ura, M., 2005. General expressions for internal deformation fields due to a dislocation source in a multilayered elastic half-space, *Geophys. J. Int.,* **161,** 507–521.

Gilbert, F. & Backus, G., 1966. Propagator matrices in elastic wave and vibration problems, *Geophysics,* **31,** 326–332.

Graig, R.F., 1997. *Soil Mechanics,* Taylor & Francis Group, London.

Han, F., 2006. Development of novel green's functions and their applications to multiphase and multilayered structures, *PhD thesis*, University of Akron.

Khazanovich, L., 1994. Structural analysis of multi-layered concrete pavement systems, *PhD thesis*, University of Illinois, Urbana, IL.

Love, A.E.H., 1944. *A Treatise on the Mathematical Theory of Elasticity,* 4th edn, Dover Publications, New York.

Lucas, S.K., 1995. Evaluation infinite integrals involving products of Bessel functions of arbitrary order, *J. Comput. Appl. Math.,* **64,** 269–282.

Lucas, S.K. & Stone, H.A., 1995. Evaluating infinite integrals involving Bessel functions of arbitrary order, *J. Comput. Appl. Math.,* **64,** 217–231.

Murthy, V.N.S., 2003. *Geotechnical Engineering: Principles and Practices of Soil Mechanics and Foundation Engineering,* Marcel Dekker, Inc., New York.

Pan, E., 1989a. Static response of a transversely isotropic and layered half-space to general dislocation sources, *Phys. Earth Planet. Inter.,* **58,** 103–117.

Pan, E., 1989b. Static response of a transversely isotropic and layered half-space to general surface loads, *Phys. Earth Planet. Inter.,* **54,** 353–363.

Pan, E., 1997. Static Green's functions in multilayered half-spaces, *Appl. Math. Model.,* **21,** 509–521.

Pan, E. & Han, F., 2005. Green's functions for transversely isotropic piezoelectric functionally graded multilayered half spaces, *Int. J. Solids Struct.,* **42,** 3207–3233.

Rice, J.R., 1983. *Numerical Methods, Software, and Analysis: IMSL Reference Edition,* McGraw-Hill Book Company, New York.

Schwarzer, N., 2000. Arbitrary load distribution on a layered half space, *J. Tribology,* **122,** 672–681.

Wang, C.D., Tzeng, C.S., Pan, E. & Liao, J.J., 2003. Displacements and stresses due to a vertical point load in an inhomogeneous transversely isotropic half-space, *Int. J. Rock Mech. Min. Sci.,* **40,** 667–685.

Yue, Z.Q. & Yin, J.H., 1998. Backward transfer-matrix method for elastic analysis of layered solids with imperfect bonding, *J. Elasticity,* **50,** 109–128.

APPENDIX A

(1) The elements of the solution matrix $[\boldsymbol{Z}(z)]$ in each layer:

$$Z_{11} = c_1 e^{\lambda z}; \quad Z_{12} = c_1 e^{-\lambda z}; \quad Z_{13} = \left(\frac{c_2}{\lambda} + c_1 z\right) e^{\lambda z}; \quad Z_{14} = \left(-\frac{c_2}{\lambda} + c_1 z\right) e^{-\lambda z},$$

$$Z_{21} = c_1 e^{\lambda z}; \quad Z_{22} = -c_1 e^{-\lambda z}; \quad Z_{23} = \left(\frac{c_3}{\lambda} + c_1 z\right) e^{\lambda z}; \quad Z_{24} = \left(\frac{c_3}{\lambda} - c_1 z\right) e^{-\lambda z},$$

$$Z_{31} = e^{\lambda z}; \quad Z_{32} = -e^{-\lambda z}; \quad Z_{33} = \left(-\frac{1}{\lambda} + z\right) e^{\lambda z}; \quad Z_{34} = \left(-\frac{1}{\lambda} - z\right) e^{-\lambda z},$$

$$Z_{41} = e^{\lambda z}; \quad Z_{42} = e^{-\lambda z}; \quad Z_{43} = z e^{\lambda z}; \quad Z_{44} = z e^{-\lambda z}, \tag{A1}$$

where c_i $(i = 1, 2, 3)$ are the material coefficients in the layer and are related to the Young's modulus E and Poisson's ratio ν as

$$c_1 = \frac{1+\nu}{E} = \frac{1}{2c_{44}}$$

$$c_2 = -\frac{2(1+\nu)(1-\nu)}{E} = \frac{-(1-\nu)}{c_{44}}.$$

$$c_3 = \frac{(1+\nu)(1-2\nu)}{E} = \frac{(1-2\nu)}{2c_{44}} \tag{A2}$$

(2) The solution matrix $[\boldsymbol{Z}^{\mathrm{N}}(z)]$ in each layer is

$$[Z^N(z)] = \begin{bmatrix} e^{\lambda z} & e^{-\lambda z} \\ c_{44} e^{\lambda z} & -c_{44} e^{-\lambda z} \end{bmatrix}. \tag{A3}$$

(3) The propagator matrix $[\boldsymbol{a}_{\mathrm{k}}]$ in layer k can be expressed as

$$[\mathbf{a}_k] = -\left(\frac{1}{c_2}\right)[\mathbf{b}_k], \tag{A4}$$

where the elements of the matrix $[\boldsymbol{b}_{\mathrm{k}}]$ are (omitting the subscript k)

$$\begin{aligned}
b_{11} &= b_{33} = -c_2 \cosh(\lambda h) - \lambda h c_1 \sinh(\lambda h) \\
b_{12} &= -b_{43} = -(c_1 + c_2) \sinh(\lambda h) - \lambda h c_1 \cosh(\lambda h) \\
b_{13} &= c_1(c_1 + 2c_2) \sinh(\lambda h) + \lambda h c_1^2 \cosh(\lambda h) \\
b_{14} &= -b_{23} = \lambda h c_1^2 \sinh(\lambda h) \\
b_{21} &= -b_{34} = c_3 \sinh(\lambda h) + \lambda h c_1 \cosh(\lambda h) \\
b_{22} &= b_{44} = (c_1 + c_3) \cosh(\lambda h) + \lambda h c_1 \sinh(\lambda h) \\
b_{24} &= -c_1(c_1 + 2c_3) \sinh(\lambda h) - \lambda h c_1^2 \cosh(\lambda h) \\
b_{31} &= -\sinh(\lambda h) + \lambda h \cosh(\lambda h) \\
b_{32} &= -b_{41} = \lambda h \sinh(\lambda h) \\
b_{42} &= -\sinh(\lambda h) - \lambda h \cosh(\lambda h)
\end{aligned} \tag{A5}$$

(4) The propagator matrix $[a_k^N]$ in layer k can be expressed as (omitting the subscript k)

$$[a_k^N] = \begin{bmatrix} \cosh(\lambda h) & -\sinh(\lambda h)/c_{44} \\ -c_{44} \sinh(\lambda h) & \cosh(\lambda h) \end{bmatrix}. \tag{A6}$$